Current Optics and Photonics
Vol. 4, No. 6, December 2020, pp. 466-471

ISSN: 2508-7266(Print) / ISSN: 2508-7274(Online)
DOI: https://doi.org/10.3807/COPP.2020.4.6.466

Comparative Measurement of Transverse Nuclear Magnetization of Polarized ^{129}Xe and ^{131}Xe by Spin-exchange Optical Pumping

Ye Jin Yu, Seong Ho Min, and Han Seb Moon*

Department of Physics, Pusan National University, Busan 46241, Korea

(Received September 29, 2020 : revised October 20, 2020 : accepted October 27, 2020)

We analyze the transverse nuclear magnetizations of ^{129}Xe and ^{131}Xe in a vapor cell containing natural Xe, ^{87}Rb, and buffer gases. The Xe atoms are polarized through spin-exchange optical pumping (SEOP) with Rb atoms under low-magnetic-field conditions. From the free-induction-decay (FID) signal, we measure the nuclear magnetization of the Xe atoms in the Xe-Rb vapor cell. Furthermore, we measure the dependence of the gyromagnetic ratio on the magnetization of ^{129}Xe and ^{131}Xe by examining the amplitude of the FID signal of each isotope, and we evaluate the relationship between the magnetic field gradient and transverse relaxation rate for both of the ^{129}Xe and ^{131}Xe isotopes.

Keywords : Nuclear magnetic resonance, Natural Xenon gas, Atomic gyro, Quantum sensor
OCIS codes : (020.1670) Coherent optical effects; (020.7490) Zeeman effect; (300.6210) Spectroscopy, atomic; (300.6260) Spectroscopy, diode lasers

I. INTRODUCTION

Atoms are considered the most suitable resource to address the increasing need for technologies for accurate measurement of physical quantities. The unique nature of the quantum states of atoms facilitates their application in atomic clocks, atomic magnetic systems, atomic spin gyroscopes, atomic interferometers, and other atomic sensors [1-9]. In particular, atomic magnetic sensors have attracted considerable research attention because of their high sensitivity, small size, low-cost implementation, and considerable development potential [6-9].

Among the various atomic magnetic sensors, the atomic spin gyroscope has high magnetic-field sensitivity and can be used as a miniaturized navigation device. Moreover, it can be implemented with the nuclear-magnetic-resonance (NMR) method [2] or the comagnetometer method [5]. NMR gyroscopes (NMRGs) measure the Larmor frequency of an atomic nucleus to determine its angular rate via its external rotation. To compensate for changes in the resonance frequency caused by magnetic field noise, high-sensitivity NMRGs use two nuclear species, ^{129}Xe and ^{131}Xe. In this context, in 2014 the Northrop Grumman Corporation developed a dual-species NMRG with a bias instability of 0.01 deg/hour for navigation purposes [3]. In 2005, the Romalis group developed another type of gyroscope technology by implementing the co-magnetometer method in the spin-exchange-relaxation-free regime under a near-zero-magnetic-field environment at high temperature, achieving a bias instability of 0.04 deg/hour [5]. They proposed a modified ^{3}He-^{129}Xe comagnetometry method with the use of ^{87}Rb to obtain a bias instability of 0.009 deg/hour in 2018 [7]. Although, there are various techniques to improve gyroscopes, such as synchronous spin-exchange optical pumping [8], dual-species NMRGs are considered the definitive solution for improving the performance of gyroscopes, and thus more research on the characteristics of dual-species system is needed.

However, the NMR signal generated by spin-exchange optical pumping (SEOP) in the case of ^{131}Xe is weaker than that of ^{129}Xe, which only entails interactions with magnetic dipoles and generates stronger spin polarization [10]. To compensate for the difference in NMR signal strength, isolated ^{129}Xe and ^{131}Xe isotopes can be used to

*Corresponding author: hsmoon@pusan.ac.kr, ORCID 0000-0003-0913-0648
Color versions of one or more of the figures in this paper are available online.

This is an Open Access article distributed under the terms of the Creative Commons Attribution Non-Commercial License (http://creativecommons.org/licenses/by-nc/4.0/) which permits unrestricted non-commercial use, distribution, and reproduction in any medium, provided the original work is properly cited.

Copyright © 2020 Current Optics and Photonics

match the NMR strength between the two isotopes, which can yield an NMRG with high accuracy and low noise [11].

Nevertheless, this approach possesses the disadvantage that the production of isolated Xe isotopes is difficult and costly; therefore, research on NMRGs based on natural Xe gas is needed. Here we note that the natural abundances of ^{129}Xe and ^{131}Xe are 26.4% and 21.1% respectively. Against this backdrop, in this paper we analyze the characteristics of ^{129}Xe and ^{131}Xe in Rb-natural Xe gas cells, with the aim of employing natural Xe gas in an NMRG. We measure the NMR signals of ^{129}Xe and ^{131}Xe through the FID method by applying a radio-frequency (RF) magnetic field pulse to the cell. We compare the amplitudes of the FID signals of both isotopes in natural-abundance Xe gas, and we observe that each isotope exhibits a different tendency according to the magnetic field inhomogeneity [12]. Through comparison and analysis of the spectroscopic characteristics of ^{129}Xe and ^{131}Xe, we expect to develop an NMRG using natural Xe gas.

II. EXPERIMENTAL SETUP

The experimental setup for optical pumping is shown in Fig. 1. The vapor consists of enriched ^{87}Rb, natural Xe (50 Torr), N_2 (250 Torr), and H_2 (5 Torr). The pump and probe lights have the same center frequency of 377 THz, which corresponds to the D_1 transition line of ^{87}Rb. The pump light is produced by an external cavity diode laser (ECDL) tuned to $|5S_{1/2}, F=2> \rightarrow |5P_{1/2}, F=1>$ by means of saturated-absorption spectroscopy (SAS), and the power is amplified with a master-oscillator power amplifier (MOPA) up to 210 mW. To generate an effective optical-interaction region, two spherical lenses are used to increase the pump beam size to a diameter of 12 mm for the complete illumination of the entire cell, which is shaped like a cube with an inner-side length of 13 mm. The vapor cell is placed inside a magnetic shielding chamber with a bias field of 6.99 μT along the z-axis, with the Larmor frequencies of ^{129}Xe and ^{131}Xe set as 82.36 Hz and 24.41 Hz respectively. The Rb atoms are pumped by left-circularly-polarized light generated by using a polarization beam splitter (PBS) and quarter-wave plate (QWP) along the propagation axis (z-axis). According to the selection rules, a limit of $\triangle m_F = 1$ is set for left-circularly-polarized light, where m_F indicates the magnetic sublevel. Optically pumped Rb atoms prepare SEOP as the $F=2$, $m_F=2$ state is populated, and subsequently transfer their electron spin to the nuclear spin of Xe by means of the hyperfine interaction, resulting in hyperpolarized Xe [13-15]. A distributed-Bragg-reflector (DBR) laser is used as the probe-light source, to exploit the wide and stable spectrum of Rb atoms. The frequency of the probe light is 2 GHz blue-detuned from $|5S_{1/2}, F=2> \rightarrow |5P_{1/2}, F=1>$, by monitoring SAS. The polarization of the probe light is linear after passing through the Glan-Thompson polarizer (GTP) positioned along the x-axis propagation direction. To avoid additional optical pumping by the probe light, the power of the probe is reduced to 5.5 mW (the beam diameter is collimated to 2 mm). After passing through the cell, the probe light enters a Wollaston prism (WP), which is tilted 45° relative to the polarization axis of GTP. The probe light is subsequently divided into two orthogonal components that undergo optical rotation in the cell, and the difference in power between the two components is measured using a balanced photodetector (BPD). When an NMR field is applied along the x-axis, phase coherence of the Xe nuclear spins is generated and nonzero transverse magnetization can be detected at the NMR frequency.

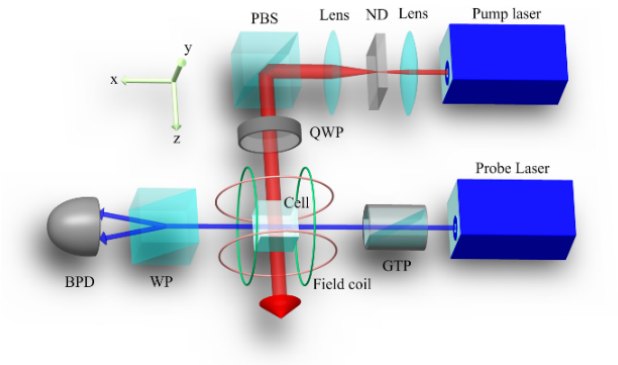
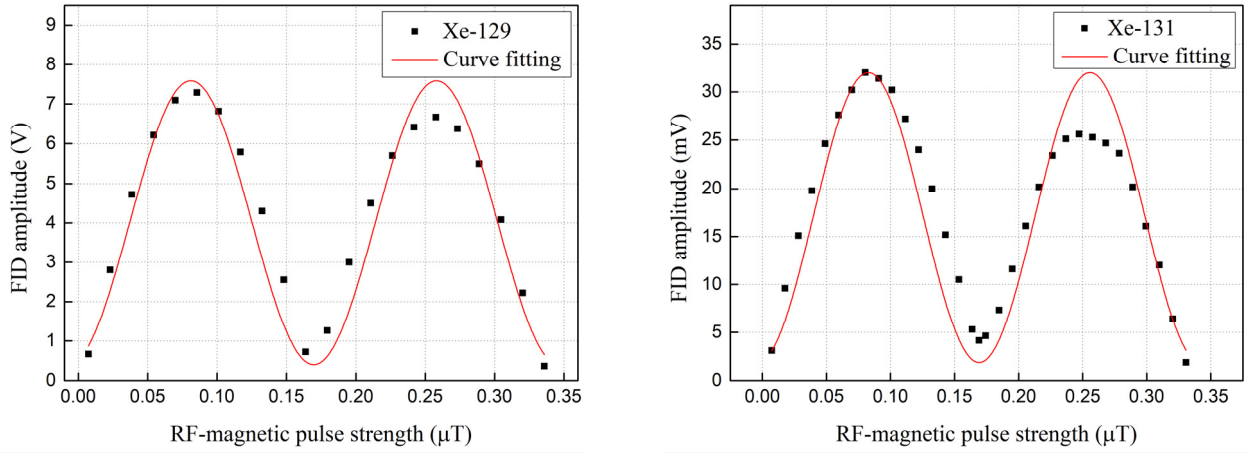


FIG. 1. Schematic diagram of the experimental setup. The natural Xe-^{87}Rb vapor cell is placed at the center of a magnetic shielding chamber surrounded by a 3-axis magnetic field coil. A bias magnetic field is applied along the z-axis while a radio-frequency pulse is applied along the x-axis. The pump laser (377 THz, D_1-line resonance frequency of Rb) is circularly polarized by means of the PBS and QWP. The linearly polarized probe-laser signals pass through the cell, and the transverse magnetization of Xe along the y-axis is read out by means of the optical-rotation signal from the combined WP-BPD detection setup (ND: neutral density filter, PBS: polarization beam splitter, Lens: spherical lens, QWP: quarter-wave plate, GTP: Glan-Thompson polarizer, WP: Wollaston prism, BPD: balanced photodetector).

III. RESULTS AND DISCUSSION

The hyperpolarized nuclear spin of Xe precesses about the axis of the bias field. Each Xe nucleus has its own phase in the precession plane (xy plane); therefore, the Xe nuclei are not in phase, resulting in zero net magnetization in the plane. An NMR RF magnetic field pulse is then applied along the x-axis to generate phase coherence of the Xe nuclei, thereby generating net magnetization in the transverse plane. When the magnetization in the transverse plane is maximum, the RF-pulse condition corresponds to a $\pi/2$ pulse. After the maximum transverse magnetization is



(a) (b)

FIG. 2. Rabi oscillations measured by means of the FID amplitudes of (a) ^{129}Xe and (b) ^{131}Xe, according to RF-pulse strength (black dots: experimental data of FID amplitude, red curve: simple sinusoidal-function fitting).

achieved with the $\pi/2$ pulse, the magnetization returns to its original, incoherent state over time; this phenomenon is named free induction decay (FID). We measured the time-varying magnetization of Rb atoms acting as an atomic magnetometer to detect the optical rotation of detuned resonant light. Figure 2 shows the FID amplitudes of ^{129}Xe and ^{131}Xe according to RF-pulse strength. The FID amplitude can be used to calculate the tilt angle θ from the z-axis to the transverse plane, according to the intensity and width of the RF-pulse [16]. This angle can be expressed as

$$\theta = -\gamma B_1 t_p/2, \tag{1}$$

where γ denotes the gyromagnetic ratio, θ the tilt angle (in radians) of the magnetization from the z-axis to the transverse plane, B_1 the magnitude of the RF-pulse, and t_p the pulse duration. In the rotating frame (x', y', z), the net magnetization rotates about the x'-axis with the x-direction RF-pulse that initially lies on the z-axis. If the magnetization direction changes by $\pi/2$ in accordance with the $\pi/2$ pulse with $t_p = \pi/\gamma B_1$, the signal is maximized in the transverse plane. However, if the angle is changed by π, the magnetization along the transverse plane is minimized, which means that the aligned nuclear spins are flipped to the opposite direction. In the measurement situation, θ is an indicator of the transverse magnetization of Xe relative to the longitudinal magnetization of Xe.

To estimate the $\pi/2$ pulse condition for each isotope, Rabi-oscillation measurements should be performed, wherein two parameters can be adjusted experimentally: B_1 and t_p. First, B_1 is fixed in both the ^{129}Xe and ^{131}Xe Rabi-oscillation measurements, to estimate the t_p of the $\pi/2$ pulse condition. When θ is fixed as $\pi/2$ with constant B_1 for both isotopes, t_p becomes inversely proportion to the γ parameter of the nucleus. The t_p values corresponding to the $\pi/2$ pulse condition with $B_1 = 0.08\,\mu T$ are 0.364 s for ^{129}Xe and 1.225 s for ^{131}Xe, which are in good agreement with the corresponding values calculated using Eq. (1). Thus we have

$$\frac{\gamma_{129}}{\gamma_{131}} = \frac{11.7774\ MHz/T}{3.4912\ MHz/T} \cong 3.37,$$
$$\frac{t_{p_{131}}}{t_{p_{129}}} = \frac{1.225\ s}{0.364\ s} \cong 3.37. \tag{2}$$

Figure 3 shows the FID signals of ^{129}Xe and ^{131}Xe as measured by the optical-rotation signal under the $\pi/2$ pulse condition; we observe an oscillating sinusoidal signal with a Larmor frequency and the amplitude of the transverse magnetization of Xe. The FID can be described by the time-varying transverse magnetization

$$M(t) = M_0 \sin(\omega_0 t) e^{-t/T_2}, \tag{3}$$

where M_0 denotes the intensity of the initial transverse magnetization, ω_0 the Larmor frequency of the Xe atom, and T_2 the transverse relaxation time. The T_2 values for the ^{129}Xe and ^{131}Xe isotopes are 15 s and 11 s respectively. Via the fast Fourier transform (FFT) of the FID, we estimate the NMRs of ^{129}Xe and ^{131}Xe to be 82.36 Hz and 24.41 Hz respectively, where the linewidths were measured as 0.045 Hz and 0.07 Hz respectively. ^{131}Xe has a nuclear spin of 3/2, which simultaneously produces magnetic dipole and electric quadrupole interactions, whereas ^{129}Xe has a nuclear spin of 1/2, which allows for only magnetic dipole interactions. The numbers of NMR energy levels of ^{131}Xe and ^{129}Xe are 4 and 2 respectively. A smaller number of energy levels can ensure greater polarizability, in terms of spin alignment; this is why the magnetization level of

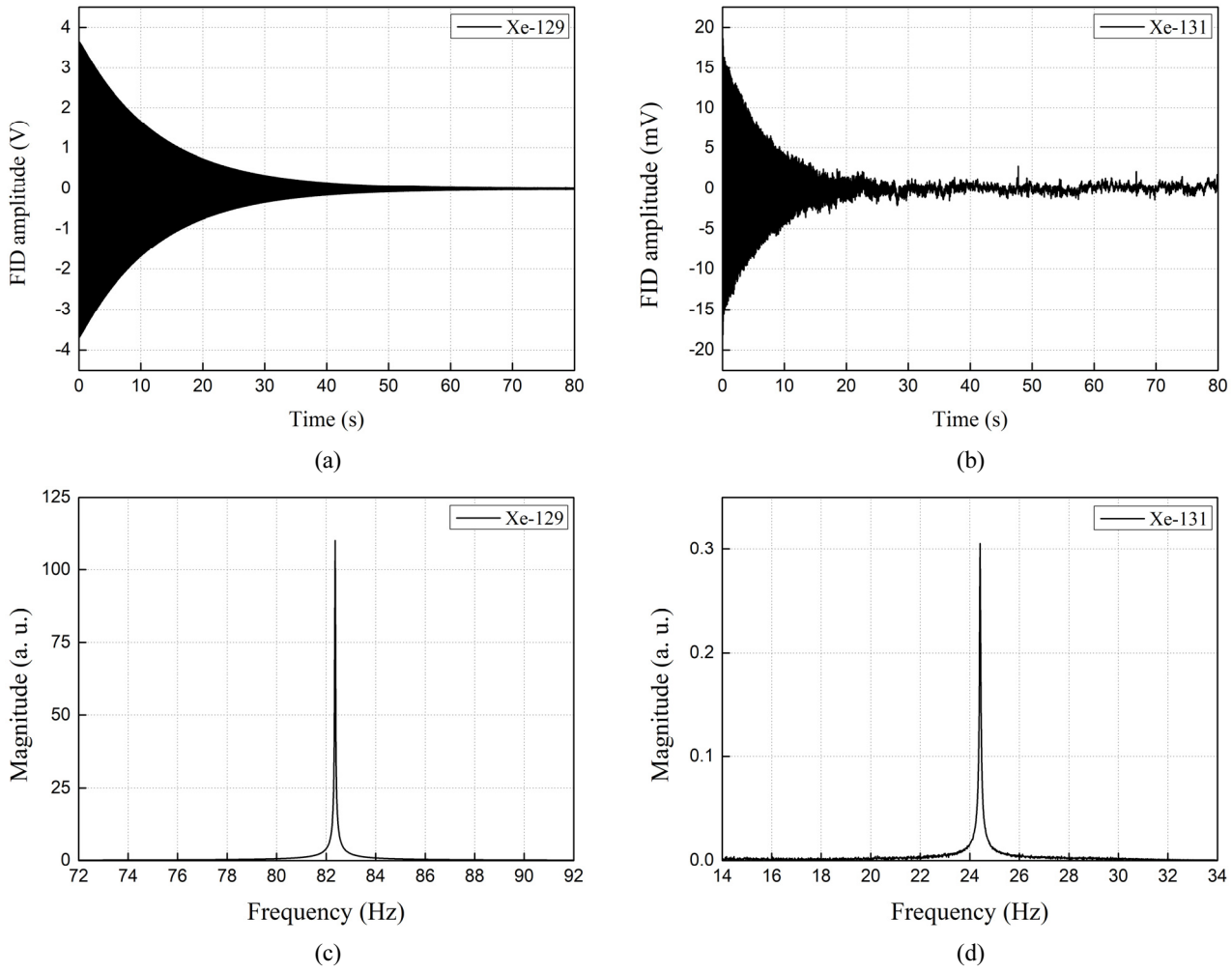


FIG. 3. FID signals of (a) ^{129}Xe and (b) ^{131}Xe for a bias-field strength of 6.99 μT, and FFT spectra obtained from the FID signals of (c) ^{129}Xe and, (d) ^{131}Xe (NMR frequency of ^{129}Xe = 82.36 Hz, NMR frequency of ^{131}Xe = 24.41 Hz).

^{131}Xe is smaller and its NMR width is broader, compared to the counterparts of ^{129}Xe. As a result, the SEOP efficiency is higher for ^{129}Xe than for ^{131}Xe. When the NMR signals of ^{129}Xe and ^{131}Xe are measured by the FID method, a difference in signal amplitude between the two isotopes is observed.

Here we note that the magnetic gradient produced in the chamber depends on the intensity of the current applied to the magnetic field coil. Exploiting this fact, we compare the transverse relaxation rates of the two Xe isotopes under different magnetic field gradients. It is noteworthy that the center of the cell is installed at the 0-cm position in the chamber. From the results shown in Fig. 4, we can confirm that the magnetic field gradient across the cell changes from 9.017 to 32.82 nT/cm. The relation of the transverse relaxation rate $\Gamma_{\delta B}(1/T_2)$ to the magnetic field gradient can be simplified as follows [12]:

$$\Gamma_{\delta B} \approx C\frac{R^4\gamma^2}{D}\left(\frac{\partial B}{\partial z}\right)^2 = C'\left(\frac{\partial B}{\partial z}\right)^2. \quad (4)$$

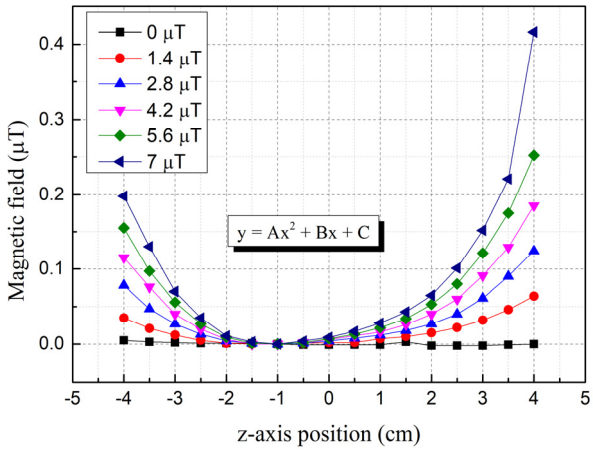


FIG. 4. Magnetic homogeneity inside the chamber along the *z*-axis, under different bias-field conditions. The *z*-axis length of the chamber is 8 cm, and the cell is positioned at the center of the chamber (black squares: zero bias *B*-field, red circles: 1.4 μT, blue triangles: 2.8 μT, magenta triangles: 4.2 μT, green diamonds: 5.6 μT, navy triangles: 7 μT).

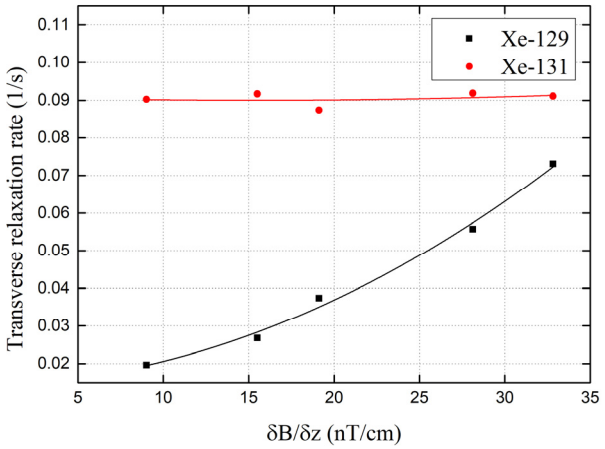


FIG. 5. Transverse relaxation rates of ^{129}Xe (black dots) and ^{131}Xe (red dots) according to magnetic field gradient. The fitting lines are calculated from Eqs. (4) and (5).

Here C denotes a constant, R the cell radius, and D the diffusion constant of the noble-gas atoms in the cell. These three coefficients are collectively represented by the term C' on the right-hand side of Eq. (4). Because ^{129}Xe and ^{131}Xe are contained in the same cell and share the same geometry and vapor pressure, R and D can be considered identical for both isotopes. Thus, $\Gamma_{\delta B}$ depends only on γ.

Figure 5 shows the measured $\Gamma_{\delta B}$ results for both isotopes. In this figure the measured $\Gamma_{\delta B}$ of ^{131}Xe indicates that there is no major change in T_2 (11 s). On the contrary, the ^{129}Xe relaxation-rate measurement indicates that the presence of a magnetic field gradient reduces T_2 (50 to 15 s) and C'_{129}. From the black curve in Fig. 5, which is fitted using polynomial curve fitting, we estimate C'_{129} as 4.87×10^{-6}. Thus we have

$$\frac{C'_{129}}{C'_{131}} = \frac{\gamma_{129}^2}{\gamma_{131}^2} = 11.38. \quad (5)$$

The C'_{131} value of ^{131}Xe, which was confirmed from Eq. (5), was substituted into Eq. (4); this value is represented by the red curve in Fig. 5. The γ value of ^{129}Xe is larger than that of ^{131}Xe; therefore, the $\Gamma_{\delta B}$ value of ^{129}Xe is more significantly affected by the square of magnetic field gradient, as in Eq. (4). When it comes to the NMRG's performance, T_2 and SNR (= transverse magnetic field noise / magnetic field of polarized Xe) directly affect on a short-term noise, known as the angle random walk ($ARW = \frac{1}{2\pi T_2 SNR}$), in which the shorter T_2 and smaller SNR of ^{131}Xe limit the ARW of the dual-species NMRG dominantly.

IV. CONCLUSION

We have compared the NMR characteristics of ^{129}Xe and ^{131}Xe, which exhibit nuclear spin in the isotopic composition of natural Xe. SEOP was used to measure the NMRs of these two isotopes under the application of a weak magnetic field. Subsequently we compared their FID amplitudes by applying different RF-pulse intensities along the x-axis direction of Xe atoms polarized along the z-axis. Consequently we estimated the ratio of each polarized Xe isotope depending on the optical pumping power under the $\pi/2$ pulse condition, and the magnetic-field-gradient sensitivities of the two Xe isotopes were observed. We expect that the findings of this study will facilitate the development of NMRGs based on natural Xe gas.

ACKNOWLEDGMENT

This work was supported by the National Research Foundation of Korea (NRF) (2018R1A2A1A19019181 and 2020M3E4A1080030); MSIT of Korea under the ITRC support program (IITP-2020-0-01606).

REFERENCES

1. J. Kitching, S. Knappe, and E. A. Donley, "Atomic sensors - a review," IEEE Sens. J. **11**, 1749-1758 (2011).
2. K. F. Woodman, P. W. Franks, and M. D. Richards, "The nuclear magnetic resonance gyroscope: a review," J. Navig. **40**, 366-384 (1987).
3. D. Meyer and M. Larsen, "Nuclear magnetic resonance gyro for inertial navigation," Gyroscopy Navig. **5**, 75-82 (2014).
4. H. Dong and Y. Gao, "Comparison of compensation mechanism between an NMR gyroscope and an SERF gyroscope," IEEE Sens. J. **17**, 4052-4055 (2017).
5. T. W. Kornack, R. K. Ghosh, and M. V. Romalis, "Nuclear spin gyroscope based on an atomic comagnetometer," Phys. Rev. Lett. **95**, 230801 (2005).
6. T. W. Kornack, "A test of CPT and Lorentz symmetry using a K-^{3}He co-magnetometer," Dr. Dissertation Princeton University, USA (2005).
7. M. E. Limes, D. Sheng, and M. V. Romalis, "^{3}He-^{129}Xe comagnetometery using ^{87}Rb detection and decoupling," Phys. Rev. Lett. **120**, 033401 (2018).
8. A. Korver, D. Thrasher, M. Bulatowicz, and T. G. Walker, "Synchronous spin-exchange optical pumping," Phys. Rev. Lett. **115**, 253001 (2015).
9. D. Budker and D. F. J. Kimball, *Optical Magnetometry* (Cambridge University Press, NY, USA, 2013), pp. 375-376.
10. E. A. Donley, J. L. Long, T. C. Liebisch, E. R. Hodby, T. A. Fisher, and J. Kitching, "Nuclear quadrupole resonances in compact vapor cells: the crossover between the NMR and the nuclear quadrupole resonance interaction regimes," Phys. Rev. A **79**, 013420 (2009).
11. A. Korver, D. Thrasher, M. Bulatowicz, and T. G. Walker, "Synchronous spin-exchange optical pumping," Phys. Rev.

Lett. **115**, 253001 (2015).
12. X. Liu, C. Chen, T. Qu, K. Yang, and H. Luo, "Transverse spin relaxation and diffusion-constant measurements of spin-polarized ^{129}Xe nuclei in the presence of a magnetic field gradient," Sci. Rep. **6**, 24122 (2016).
13. E. J. Eklund, "Microgyroscope based on spin-polarized nulcei," Ph. D. Dissertation, University of California, USA (2008).
14. T. G. Walker and W. Happer, "Spin-exchange optical pumping of noble-gas nuclei," Rev. Mod. Phys. **69**, 629 (1997).
15. A.-M. Oros and N. J. Shah, "Hyperpolarized xenon in NMR and MRI," Phys. Med. Biol. **49**, R105 (2004).
16. M. Fox, *Quantum Optics* (Oxford University Press, NY, USA, 2006), pp. 339-345.